

The giant luminous arc Statistics.

II. spherical lens models based on ROSAT HRI data.

Kohji Molikawa¹, Makoto Hattori¹, Jean-Paul Kneib², and Kazuyuki Yamashita³

¹ Astronomical Institute, Graduate School of Science, Tôhoku University, Sendai, Miyagi 980-8578, Japan

² Observatoire Midi-Pyrénées, Laboratoire d'Astrophysique, 14 Av. E. Belin, 31400 Toulouse, France

³ Information Processing Center, Chiba University, Inage, Chiba 263-8522, Japan

Received / Accepted

Abstract. We present *ROSAT HRI* X-ray observations of all the galaxy clusters in the Le Fèvre et al. arc survey sample in order to study the spatial distribution of the intra-cluster medium (ICM), and examine the expected number of giant luminous arcs for the sample using two spherically symmetric lens models constrained by our X-ray data. *Isothermal β model* assumes that the ICM is isothermal and is in the hydrostatic equilibrium. *ENF98-NFW model* assumes that the ‘universal’ dark matter halo profile proposed by Navarro, Frenk & White is a valid description of the underlying dark matter distribution. Adopting the result of N-body/gas-dynamical simulations by Eke, Navarro & Frenk, dark matter distribution in the *ENF98-NFW model* can be constrained by the X-ray surface brightness distribution of the ICM. The expected number of giant luminous arcs in the sample is then calculated taking into account both detection conditions in the arc survey and the evolution of source galaxies. We find that the *isothermal β model* cannot reproduce the observed number of giant luminous arcs even allowing uncertainties in the source galaxy model. The *ENF98-NFW model* displays good agreement in number of giant luminous arcs. However, some clusters have their virial temperature 3–4 times higher than their X-ray temperature obtained from spectral data or from the $L_X - T$ relation. Thus, we conclude that both spherical models which are consistent with all the available X-ray data cannot reproduce the observed number of giant luminous arcs in the sample. To solve this discrepancy we believe that the giant luminous arc statistics will need to take properly into account ‘irregularity’ in the mass distribution in each cluster.

Key words: Galaxies: clusters: general – Galaxies: statistics – Cosmology: observations – (*Cosmology:*) gravitational lensing – X-rays: galaxies

1. Introduction

A number of Giant luminous arcs (GLAs) have now been detected in many distant clusters of galaxies (e.g. Soucail et al. 1987; Lynds & Petrosian 1986; Fort & Mellier 1994 for a review). Their spectroscopic confirmations as lensed normal distant galaxies (e.g. Soucail et al. 1988) lead to exciting new cosmological developments in this decade.

Probing the mass distribution of distant clusters is one of avenues of these developments (e.g. Narayan & Bartelmann 1995; Hattori et al. 1999; Umetsu et al. 1999). Early analyses pointed out discrepancy of a factor 2 – 3 between cluster masses derived from strong lensing and standard X-ray analysis of the ICM (e.g. Loeb & Mao 1994; Miralda-Escudé & Babul 1995). Several possible solutions are proposed: (i) Loeb & Mao 1994 proposed that non-thermal pressure due to equipartition magnetic field and turbulent may play an important role on supporting the ICM. (ii) A multi-phase model of the ICM in the central part of clusters – indicated by the cooling flow model (Allen et al. 1996) – increases by a factor 2–3 the mass deduced from X-ray compared to standard (single-phase) isothermal model (Allen 1998). (iii) Leaving from “inappropriate modeling of the cluster mass distribution due to neglecting the contributions by substructure and member galaxies, which leads overestimation of the cluster mass from strong lensing events (e.g. Kneib et al. 1993; Kneib et al. 1995; Kneib et al. 1996; Hattori et al. 1998). One can expect that the next generation X-ray telescopes (Chandra, XMM, Astro-E) will provide definite answer of the first two possible solutions. The third one seems, however, the closest one to the reality (Hattori et al. 1999).

Instead of these detailed analyses for individual clusters, Statistics of GLAs constrains the average properties of cluster mass distribution. The statistics of GLAs is consist in counting the number of GLAs in a well defined cluster sample and constrains the average properties of cluster mass distribution. Using spherically symmetric mass distribution models, Wu & Hammer (1993) showed that the predicted number of GLAs was critically dependent on the degree of the central mass concentration of clusters.

Miralda-Escudé (1993a) examined arc statistics with elliptical lens models and concluded that elliptical mass distribution did not change the above conclusion drastically. Using numerically simulated model for clusters, Bartelmann and his collaborators (Bartelmann & Weiss 1994; Bartelmann et al. 1995, henceforth BSW95) showed that their asymmetric cluster mass distribution (e.g. substructure) increased the expected number of GLAs. In a further study, Bartelmann et al. (1998) examined the dependence of arc statistics on cosmological parameters. They concluded that the open cold dark matter model gave the largest number of giant arcs compared to other cosmology, in particular the Einstein-de Sitter universe and that the open cold dark matter model was likely to be the only model which could match current observations.

The first well-defined GLA survey was conducted by Le Fèvre et al (1994, henceforth LF94). Hattori et al. (1997, henceforth Paper I) proposed a method that predicted the number of GLAs taking into account both detection conditions in the arc survey and the evolution of source galaxies. They applied their method to the LF94 arc survey sample using the *Einstein* X-ray data to calibrate the mass distribution - assuming the hydrostatic equilibrium and the spherical symmetry. The conclusion of Paper I is that the expected number of GLAs deduced from the X-ray analysis was inconsistent with the observed one. Hamana & Futamase (1997, henceforth HF97) examined the GLA statistics taking into account the evolution of the luminosity function found by the Canada France Redshift Survey (Lilly et al. 1995). They showed that the observed evolution in the galaxy luminosity function increased the expected GLA number by a factor of 2 – 3 at most. Although the $L_X - \sigma$ relation adopted by them and by Wu & Hammer (1993) appeared to be incorrect when compared with recent results (e.g. Mushotzky & Scharf 1997; Markevitch 1998), we can study how sensitive the GLA statistics is on the evolution of the galaxy luminosity function.

This paper is the second in a series on the giant luminous arc statistics with the LF94 arc survey sample. In this paper we re-visit the LF94 sample with higher quality *ROSAT HRI* data because no precise measurements of the ICM spatial distribution in the LF94 sample clusters were available in Paper I. We assume that the mass distribution in clusters are spherically symmetric. This paper is organized as follows. In §4, we describe the lensing properties of mass models. We discuss the GLA statistics and its implication in §5, and summarize our conclusion in §6. Notes on individual clusters, as well as contour plot and radial profile of each cluster, are given in the appendix. Throughout this paper, we adopt a Hubble constant of $H_0 = 50h_{50} \text{ km s}^{-1} \text{ Mpc}^{-1}$, the present density parameter of $\Omega_{m0} = 0.3$, and the present cosmological parameter of $\Omega_{\Lambda0} = 0.7$.

2. Cluster sample and its X-ray data

2.1. Cluster sample and its X-ray observations

Selecting 16 distant and rich clusters with $L_X(0.3 - 3.5\text{keV}) > 4 \times 10^{44} \text{ erg s}^{-1}$ ($H_0 = 50h_{50} \text{ km s}^{-1} \text{ Mpc}^{-1}$, $\Omega_{m0} = 1.0$, $\Omega_{\Lambda0} = 0.0$ and $z > 0.2$) from a complete sample of distant rich clusters selected from the EMSS, LF94 performed a medium-deep *V, R*, and *I* imaging for a GLA survey and found 6 GLAs.

X-ray observations for all the 16 clusters in the LF94 sample were performed by *ROSAT HRI*. The *HRI* data of 11 clusters were taken from the ROSAT Archive at Max-Planck-Institut für extraterrestrische Physik (MPE). The *HRI* data of remaining clusters were obtained by our own proposals. The instrument *HRI* had $\sim 5''$ FWHM resolution and was sensitive for an energy range of 0.1 – 2.4 keV (Trümper 1984), which makes *HRI* the best instrument to date to perform detailed observation of the ICM distribution in distant clusters. In Table 1, we list the log of the *ROSAT HRI* observations. The column density of the galactic hydrogen in 6th column in the Table 1 is calculated using *EXSAS*¹ command ‘CALCULATE/GALACTIC_NH’ which calculates the galactic hydrogen column density toward the specified direction and is based on Dickey & Lockman (1990). Our observation revealed that MS 1333.3+1725 was *not* a cluster but an X-ray point source.

2.2. ROSAT HRI data reduction

We used *EXSAS* and *XSPEC*² analysis packages to reduce the data. The position of point sources higher than 3σ is determined via standard source detection pipeline for *HRI* data in *EXSAS*. The cluster center was determined as the brightest X-ray peak. Accuracy of *ROSAT HRI* pointing was checked with both Hambrug RASS Catalog of Optical ID (HRASSCAT) and ROSAT SIMBAD identifications (ROSID)³. Positions of sources higher than 3σ were compared with positions of objects cataloged in HRASSCAT or ROSID. The vignetting of the *ROSAT HRI* was less than 5% within a radius of 5 arcminutes (i.e. 600 pixels) from the detector center at all energy range of 0.1 – 2.4 keV for which the *ROSAT HRI* was sensitive. Thus we restricted our analysis to the inner 600 pixels of each image, where the background can be regarded as flat.

2.3. Data analyses

Photon event tables were binned into radial rings to make azimuthally averaged surface brightness profiles.

¹ Extended Scientific Analysis System provided by ROSAT Science Data Center at MPE

² provided by NASA/Goddard Space Flight Center.

³ both are available via High Energy Astrophysics Science Archive Research Center (HEASARC) Online Service, provided by NASA/Goddard Space Flight Center. http://heasarc.gsfc.nasa.gov/docs/frames/mb_w3browse.html

Table 1. The log of *ROSAT HRI* observations of the sample clusters.

Cluster name	Redshift	Pointing R.A. (J2000.0)	Pointing Dec. (J2000.0)	Observation date	Exposure [ksec.]	Column density [10^{21} cm $^{-2}$]
MS 0015.9+1609	0.546	00 ^h 18 ^m 33 ^s .6	+16°26'24"	95 Jan 09 – 95 Jul 05	76.1	0.41
MS 0302.7+1658	0.426	03 ^h 05 ^m 33 ^s .6	+17°10'12"	95 Aug 19 – 95 Aug 27	33.8	1.07
MS 0353.6–3642	0.320	03 ^h 55 ^m 31 ^s .2	-36°33'36"	94 Jul 19 – 94 Aug 21	22.2	0.12
MS 0451.5+0250	0.202	04 ^h 54 ^m 09 ^s .6	+02°55'12"	94 Mar 05 – 94 Mar 06	12.7	0.78
MS 0735.6+7421	0.216	07 ^h 41 ^m 50 ^s .4	+74°15'00"	92 Mar 14 – 92 Apr 21	27.0	0.41
MS 1006.0+1202	0.221	10 ^h 08 ^m 45 ^s .6	+11°48'00"	96 Jun 03 – 96 Dec 06	22.4	0.37
MS 1008.1–1224	0.301	10 ^h 10 ^m 33 ^s .6	-12°39'36"	94 May 16 – 94 Jun 17	68.7	0.73
MS 1224.7+2007	0.327	12 ^h 27 ^m 14 ^s .4	+19°51'00"	94 Jun 20 – 96 Jun 05	37.1	0.29
MS 1333.3+1725	0.460	13 ^h 35 ^m 48 ^s .0	+17°09'36"	97 Jul 11 – 97 Jul 24	54.4	0.18
MS 1358.4+6245	0.328	13 ^h 59 ^m 50 ^s .3	+62°31'12"	91 Nov 05 – 93 May 15	29.2	0.19
MS 1455.0+2232	0.259	14 ^h 57 ^m 14 ^s .4	+22°20'24"	92 Jan 11 – 94 Jul 08	14.8	0.33
MS 1512.4+3647	0.372	15 ^h 14 ^m 24 ^s .0	+36°36'36"	95 Feb 06 – 95 Feb 06	35.0	0.14
MS 1621.5+2640	0.426	16 ^h 23 ^m 36 ^s .0	+26°33'36"	94 Jul 28 – 94 Jul 30	43.8	0.36
MS 1910.5+6736	0.246	19 ^h 10 ^m 28 ^s .8	+67°41'24"	96 Feb 22 – 96 Mar 04	25.1	0.60
MS 2053.7–0449	0.583	20 ^h 56 ^m 21 ^s .6	-04°37'48"	96 May 07 – 96 May 06	4.9	0.50
MS 2137.3–2353	0.313	21 ^h 40 ^m 12 ^s .0	-23°39'36"	92 Nov 26 – 94 Apr 25	15.5	0.36

The width of each ring was determined in order that the number of photons in each bin become greater than or equal to 25 to ensure that χ^2 fitting could be performed, and that the size of each bin become greater than or equal to $2.5'' \sim \text{FWHM}/2$. A radial surface brightness profile was then constructed by summing up the counts in each bin. Note that all the contaminating point sources which were higher than 3σ were excluded from the photon counting.

The radial surface brightness profile was fitted via χ^2 -minimization routine to (Cavaliere and Fusco-Femiano 1976)

$$S(\theta) = S_0 \left[1 + \left(\frac{\theta}{\theta_c} \right)^2 \right]^{-3\beta_{\text{fit}}+1/2} + B, \quad (1)$$

where S_0 is the central surface brightness, θ_c is the angular core radius, and B is the background. It was physically interpreted that β_{fit} described the ratio of the kinetic energy per unit mass of the member galaxy to that in the ICM if cluster galaxy and the ICM distributions are isothermal and galaxy velocity dispersion is isotropic. Therefore, the surface brightness distribution described by the Eq. (1) was called isothermal β model. However, it seems that such a situation is far from the reality (Lubin & Bahcall 1993; Bahcall & Lubin 1994). Therefore, Eq. (1) has no meaning more than a conventional fitting model. We call the model β described by the Eq. (1) ‘standard β model’ in this paper. The background value was first determined via the above fitting. Removing the background from the image we then checked that the radial source photon counts remained constant outside the cluster source region, if not we modified the background value accordingly, and we redid the standard β model fitting. In Table 2, we list the

standard β model fitting result. The bracketed numbers in 6th column is the edge within which source photon numbers are counted.

2.4. X-ray properties of the sample clusters

We list fluxes, luminosities and temperatures of the sample clusters calculated using the best-fit values of the standard β model fitting on the left side of each column in Table 2. Fluxes in the 0.1 – 2.4 keV band were calculated on the XSPEC using Raymond-Smith thermal plasma model assuming 30% of solar metallicity. The calculation of the flux requires the value of the temperature. For clusters who have no ASCA observation, the temperature of 6 keV was first assumed and the temperature was calculated iteratively using the 2–10 keV X-ray luminosity–temperature ($L_X - T$) relation of Arnaud & Evrard (1998, henceforth AE98) until the temperature converges. When ASCA temperature (T_{ASCA}) was available, we used it to compute the X-ray flux and luminosity of the clusters. This luminosity was then used to compute the expected temperature from the $L_X - T$ relation (we specify this in Table 4 by bracketing the temperatures with parentheses in column 6).

Although the $L_X - T$ relation of AE98 was derived from nearby cluster sample, we used it for our distant cluster sample assuming no evolution of $L_X - T$ relation. David et al. (1993, henceforth D93) also derived 2–10 keV $L_X - T$ relation in $(\Omega_{m0}, \Omega_{\Lambda0}) = (0, 0)$ cosmology using Raymond-Smith thermal plasma model but they assumed 50 % of solar metallicity which is too high value for the ICM. Since AE98 showed the $L_X - T$ relation in $(\Omega_{m0}, \Omega_{\Lambda0}) = (1, 0)$ cosmology, we re-plotted the $L_X - T$

Table 2. The result of standard β model fitting.

Cluster name	S_0 [count s^{-1} $arcsec^{-2}$]	β_{fit}	θ_c^*	Background [count s^{-1} $arcsec^{-2}$]	$\chi^2/d.o.f.$	count rate [count s^{-1}]
MS 0015.9+1609	$4.38^{+0.54}_{-0.48} \times 10^{-6}$	$0.72^{+0.12}_{-0.08}$	$42.8^{+9.6}_{-7.4}''$ $382h_{50}^{-1}$ kpc	$9.88 \times 10^{-7}^\dagger$	113.34/116 = 0.98	0.0344 ($\leq 182''$)
MS 0302.7+1658	$6.68^{+7.58}_{-2.14} \times 10^{-6}$	$0.62^{+0.34}_{-0.13}$	$11.3^{+9.5}_{-6.6}''$ $88h_{50}^{-1}$ kpc	$1.16 \times 10^{-6}^\dagger$	77.97/84 = 0.93	0.00871 ($\leq 221''$)
MS 0353.6-3642	$5.35^{+1.27}_{-1.05} \times 10^{-6}$	$0.62^{+0.28}_{-0.13}$	$31.9^{+18.8}_{-10.6}''$ $208h_{50}^{-1}$ kpc	$9.19^{+0.38}_{-0.50} \times 10^{-7}$	112.34/113 = 0.99	0.0449 ($\leq 231''$)
MS 0451.5+0250	$2.94^{+0.41}_{-0.35} \times 10^{-6}$	$0.74^{+0.32}_{-0.15}$	$126.0^{+55.2}_{-33.7}''$ $587h_{50}^{-1}$ kpc	$1.16 \times 10^{-6}^\dagger$	100.11/110 = 0.91	0.158 ($\leq 293''$)
MS 0735.6+7421	$5.20^{+0.95}_{-0.85} \times 10^{-5}$	$0.48^{+0.02}_{-0.01}$	$8.5^{+1.5}_{-1.2}''$ $42h_{50}^{-1}$ kpc	$1.25 \times 10^{-6}^\dagger$	159.63/117 = 1.36	0.0945 ($\leq 279''$)
MS 1006.0+1202	$2.72^{+0.30}_{-0.27} \times 10^{-6}$	$0.91^{+0.29}_{-0.16}$	$82.9^{+24.8}_{-16.4}''$ $414h_{50}^{-1}$ kpc	$1.30 \times 10^{-6}^\dagger$	148.30/115 = 1.29	0.0437 ($\leq 155.5''$)
MS 1008.1-1224	$3.91^{+0.76}_{-0.61} \times 10^{-6}$	$0.63^{+0.11}_{-0.07}$	$36.4^{+11.5}_{-8.6}''$ $228h_{50}^{-1}$ kpc	$1.22 \times 10^{-6}^\dagger$	166.06/116 = 1.43	0.0333 ($\leq 183''$)
MS 1224.7+2007	$1.07^{+0.57}_{-0.39} \times 10^{-5}$	$0.47^{+0.07}_{-0.05}$	$6.6^{+4.0}_{-2.7}''$ $44h_{50}^{-1}$ kpc	$1.25 \times 10^{-6}^\dagger$	115.92/112 = 1.04	0.0179 ($\leq 170''$)
MS 1333.3+1725	<i>Not a cluster of galaxies</i>					
MS 1358.4+6245	$2.86^{+0.83}_{-0.68} \times 10^{-5}$	$0.47^{+0.02}_{-0.02}$	$7.2^{+2.2}_{-1.6}''$ $48h_{50}^{-1}$ kpc	$1.24 \times 10^{-6}^\dagger$	128.13/116 = 1.10	0.0484 ($\leq 212''$)
MS 1455.0+2232	$9.60^{+1.36}_{-1.24} \times 10^{-5}$	$0.64^{+0.04}_{-0.03}$	$12.3^{+1.8}_{-1.6}''$ $69h_{50}^{-1}$ kpc	$1.34 \times 10^{-6}^\dagger$	154.46/117 = 1.32	0.102 ($\leq 114''$)
MS 1512.4+3647	$2.01^{+0.58}_{-0.45} \times 10^{-5}$	$0.59^{+0.10}_{-0.06}$	$9.4^{+3.4}_{-2.5}''$ $68h_{50}^{-1}$ kpc	$1.19 \times 10^{-6}^\dagger$	90.64/117 = 0.77	0.0178 ($\leq 129''$)
MS 1621.5+2640	$3.74^{+0.62}_{-0.58} \times 10^{-6}$	117.1	$1246.8''$	$4.04 \times 10^{-6}^\dagger$	107.36/114 = 0.94	0.051 ($\leq 166''$)
MS 1910.5+6736	$3.25^{+1.17}_{-0.81} \times 10^{-6}$	$0.66^{+0.27}_{-0.12}$	$9739h_{50}^{-1}$ kpc	$29.0^{+18.5}_{-10.3}''$	7.20 $\times 10^{-7}^\dagger$ = 1.11	127.30/115 ($\leq 208''$)
MS 2053.7-0449	$\leq 1.1 \times 10^{-5}$	$2/3^\ddagger$...	$1.30 \times 10^{-6}^\dagger$...	≤ 0.00111
MS 2137.3-2353	$1.36^{+0.23}_{-0.20} \times 10^{-4}$	$0.63^{+0.04}_{-0.03}$	$8.4^{+1.4}_{-1.2}''$ $54h_{50}^{-1}$ kpc	$1.22^{+0.03}_{-0.03} \times 10^{-6}$	111.01/114 = 0.97	0.0728 ($\leq 119''$)

† Fixed. See Sec. 2.4.

‡ Assumed to estimate the upper limit of S_0 .

diagram in $(\Omega_{m0}, \Omega_{\Lambda0}) = (0.3, 0.7)$ cosmology. The $L_X - T$ relation we used is $T_X = 10^a L_X^b$, where T_X is X-ray temperature in keV and L_X is 2–10 keV X-ray luminosity in erg s^{-1} , and where $(a, b) = (-12.47 \pm 0.72, 0.296 \pm 0.016)$. As AE98 discussed, their $L_X - T$ relation has the slope of $1/2.88 = 0.347$ steeper than D93 but the $L_X - T$ relation of AE98 in $(\Omega_{m0}, \Omega_{\Lambda0}) = (0.3, 0.7)$ cosmology is rather consistent with D93. Mushotzky & Scharf (1997) reported the $L_X - T$ relation for distant clusters and showed that there was no evolution of $L_X - T$ relation up to $z = 0.5$ comparing with the sample of D93. In Table 5, we list central electron number densities (n_{e0}), central cooling times (t_{cool}), ages of the universe at the cluster's redshift (t_{age}), cooling radii (θ_{cool}), and mass-flow rates (\dot{M}_{cool}) for sample clusters. The central electron number density was calculated using rest frame 0.5–2.0 keV *HRI* luminosity assuming the gaunt factor of $0.9[h\nu/(k_B T_X)]^{-0.3}$ (Henry

& Henriksen 1997), where h is the Plank constant, ν is the frequency, k_B is the Boltzmann constant, and T_X is the X-ray temperature, and one-ninth of the hydrogen number density for the helium number density is assumed. The cooling radius is defined as the radius where $t_{cool} = t_{age}$. The cooling mass-flow rate was calculated using Eq. (2) in Fabian (1994).

3. Cluster mass models and their lens properties

In this section, we summarize lens properties of three basic cluster mass distribution models.

3.1. The singular isothermal sphere (SIS) model

Although we do not use the SIS model, the SIS model is employed by HF97 and then we give its lens properties

Table 3. The result of ENF98 β model fitting.

Cluster name	S_0 [count s^{-1} arcsec $^{-2}$]	θ_c^*	Background [count s^{-1} arcsec $^{-2}$]	$\chi^2/\text{d.o.f.}$	count rate [count s^{-1}]
MS 0015.9+1609	$4.21_{-0.38}^{+0.41} \times 10^{-6}$	$48.0_{-2.8}^{+3.0}''$ $429h_{50}^{-1}\text{kpc}$	$9.88 \times 10^{-7}^\dagger$	$114.33/117 = 0.98$	0.0344 ($\leq 182''$)
MS 0302.7+1658	$6.85_{-2.05}^{+2.44} \times 10^{-6}$	$15.2_{-2.8}^{+3.7}''$ $119h_{50}^{-1}\text{kpc}$	$1.15_{-0.02}^{+0.02} \times 10^{-6}$	$104.45/114 = 0.92$	0.00985 ($\leq 221''$)
MS 0353.6-3642	$4.71_{-0.74}^{+0.82} \times 10^{-6}$	$45.6_{-4.5}^{+5.0}''$ $297h_{50}^{-1}\text{kpc}$	9.20×10^{-7}	$116.11/115 = 1.01$	0.0449 ($\leq 231''$)
MS 0451.5+0250	$2.90_{-0.29}^{+0.31} \times 10^{-6}$	$135.1_{-9.3}^{+10.1}''$ $629h_{50}^{-1}\text{kpc}$	$1.16 \times 10^{-6}^\dagger$	$100.23/111 = 0.90$	0.158 ($\leq 293''$)
MS 0735.6+7421	$1.38_{-0.17}^{+0.19} \times 10^{-5}$	$39.1_{-3.1}^{+3.3}''$ $192h_{50}^{-1}\text{kpc}$	$1.25 \times 10^{-6}^\dagger$	$297.63/118 = 2.52$	0.0945 ($\leq 279''$)
MS 1006.0+1202	$2.83_{-0.24}^{+0.26} \times 10^{-6}$	$70.7_{-4.1}^{+4.4}''$ $353h_{50}^{-1}\text{kpc}$	$1.30 \times 10^{-6}^\dagger$	$149.78/116 = 1.29$	0.0437 ($\leq 155.5''$)
MS 1008.1-1224	$3.34_{-0.37}^{+0.40} \times 10^{-6}$	$52.0_{-3.9}^{+4.2}''$ $325h_{50}^{-1}\text{kpc}$	$1.22 \times 10^{-6}^\dagger$	$170.88/117 = 1.46$	0.0333 ($\leq 183''$)
MS 1224.7+2007	$6.69_{-2.93}^{+3.65} \times 10^{-6}$	$18.0_{-4.6}^{+8.5}''$ $119h_{50}^{-1}\text{kpc}$	$1.25 \times 10^{-6}^\dagger$	$130.19/113 = 1.15$	0.0179 ($\leq 170''$)
MS 1333.3+1725		<i>Not a cluster of galaxies</i>			
MS 1358.4+6245	$8.30_{-1.38}^{+1.66} \times 10^{-6}$	$34.1_{-3.8}^{+4.2}''$ $226h_{50}^{-1}\text{kpc}$	1.24×10^{-6}	$190.23/117 = 1.63$	0.0484 ($\leq 212''$)
MS 1455.0+2232	$7.57_{-0.84}^{+0.91} \times 10^{-5}$	$18.2_{-1.1}^{+1.2}''$ $102h_{50}^{-1}\text{kpc}$	$1.34 \times 10^{-6}^\dagger$	$177.84/118 = 1.51$	0.102 ($\leq 114''$)
MS 1512.4+3647	$1.60_{-0.30}^{+0.34} \times 10^{-5}$	$15.4_{-1.9}^{+1.9}''$ $111h_{50}^{-1}\text{kpc}$	$1.19 \times 10^{-6}^\dagger$	$97.89/118 = 0.83$	0.0178 ($\leq 129''$)
MS 1621.5+2640 [#]	$4.45_{-0.79}^{+0.89} \times 10^{-6}$	$63.6_{-8.0}^{+8.8}''$ $497h_{50}^{-1}\text{kpc}$	$4.04 \times 10^{-6}^\dagger$	$117.59/115 = 1.02$	0.051 ($\leq 166''$)
MS 1910.5+6736	$2.87_{-0.52}^{+0.61} \times 10^{-6}$	$38.0_{-4.8}^{+5.2}''$ $206h_{50}^{-1}\text{kpc}$	$7.20 \times 10^{-7}^\dagger$	$128.24/116 = 1.11$	0.0167 ($\leq 208''$)
MS 2053.7-0449	1.30×10^{-6}
MS 2137.3-2353	$1.08_{-0.15}^{+0.16} \times 10^{-4}$	$12.7_{-0.9}^{+1.0}''$ $82h_{50}^{-1}\text{kpc}$	$1.22 \times 10^{-6}^\dagger$	$132.90/115 = 1.16$	0.0728 ($\leq 119''$)

† Fixed. See Sec. 2.4.

to compare with those of lens models we employed. The density profile of a cluster described by the SIS model is

$$\rho_{\text{SIS}}(r) = \frac{\sigma^2}{2\pi G} \frac{1}{r^2}, \quad (2)$$

where σ^2 is the velocity dispersion of the cluster. The lens equation of the SIS model thereby becomes

$$y = x - \frac{x}{|x|}, \quad (3)$$

where y [x] is the angle between a source [an image] and the lens center in the unit of the Einstein ring radius of SIS model θ_E^{SIS} :

$$\theta_E^{\text{SIS}} = 4\pi \frac{\sigma^2}{c^2} \frac{D_{LS}}{D_{OS}}, \quad (4)$$

where D_{LS} [D_{OS}] is the angular diameter distance from the lens [the observer] to the source.

If we assume all background sources circular, length-to-width ratio of a GLA equals to the ratio of the tangential stretching rate to the radial stretching rate or vice versa. (As one can see in the lens equation, the radial stretching rate of the SIS model is always unity.) The moduli of the eigenvalues of the Jacobian matrix of the lens mapping are

$$\lambda_t(\text{tangential}) \equiv \left| \frac{\theta_S}{\theta_I} \right| = \left| 1 - \frac{1}{x} \right| = \left| 1 - \frac{\theta_E}{\theta_I} \right|, \quad (5)$$

$$\lambda_r(\text{radial}) \equiv \left| \frac{d\theta_S}{d\theta_I} \right| = 1. \quad (6)$$

and the length-to-width ratio of an arc is described as

$$R \equiv \frac{L}{W} = \frac{\lambda_r}{\lambda_t} = \left| 1 - \frac{\theta_E}{\theta_I} \right|^{-1}. \quad (7)$$

Table 4. Flux, luminosity and temperature of the sample clusters.

Cluster name	Flux (0.1 – 2.4 keV)		Luminosity (2 – 10 keV)		Temperature [†]		Temperature [‡] [keV]
	standard*	ENF98**	standard*	ENF98**	standard*	ENF98**	
MS 0015.9+1609	13.0		40.7		(11.1)		8.0 ^{+1.0} _{-1.0} [#]
MS 0302.7+1658	3.3	3.8	6.7	7.7	6.5	6.8	...
MS 0353.6–3642	16.2		13.4		(8.0)		8.13 ^{+2.6} _{-1.7} [#]
MS 0451.5+0250	62.1		26.7		9.8		...
MS 0735.6+7421	36.1		14.8		8.2		...
MS 1006.0+1202	16.4		6.1		6.3		...
MS 1008.1–1224	12.8		11.4		(7.6)		7.29 ^{+2.5} _{-1.5} [#]
MS 1224.7+2007	6.4		4.3		(5.7)		4.3 ^{+0.7} _{-0.6} ^b
MS 1333.3+1725	0.88 [‡]		0.12 [‡]	
MS 1358.4+6245	17.6		13.2		(7.9)		6.50 ^{+0.7} _{-0.7} [#]
MS 1455.0+2232	37.6		17.9		(8.7)		5.45 ^{+0.3} _{-0.3} [#]
MS 1512.4+3647	6.1		4.3		(5.7)		3.57 ^{+1.3} _{-0.7} [#]
MS 1621.5+2640	19.5		38.5		10.9		...
MS 1910.5+6736	6.2		2.8		5.0		...
MS 2053.7–0449	≤ 0.597		≤ 0.659		≤ 3.7		...
MS 2137.3–2353	26.4		16.7		(8.5)		4.37 ^{+0.4} _{-0.3} [#]

* From standard β model (See Sec. 2.3) fitting results.

** From ENF98 β model (See Sec. 3.3) fitting results.

† From the luminosity-temperature relation in Arnaud & Evrard (1998). See Sec. 2.4.

‡ From ASCA observations.

From Mushotzky & Scharf (1997).

b From Henry (1997).

‡ Power law model with photon index of 1.8.

Following Wu & Hammer (1993), a giant arc is defined as the image which has

$$R \geq \epsilon_{\text{th}} \equiv 10, \quad (8)$$

where ϵ_{th} is the threshold value of length-to-width ratio for identifying a giant arc (Paper I). The position of arc to be giant has to fulfill the following inequalities:

$$0 < |\theta_I| \leq \max\left(\frac{\epsilon_{\text{th}}}{\epsilon_{\text{th}} - 1}\theta_E, \frac{\epsilon_{\text{th}}}{\epsilon_{\text{th}} + 1}\theta_E\right) = \frac{\epsilon_{\text{th}}}{\epsilon_{\text{th}} - 1}\theta_E. \quad (9)$$

The cross section in the source plane for forming arcs with $R \geq \epsilon_{\text{th}}$ hence reads

$$\sigma_G^{\text{SIS}} = \pi \left(\frac{D_{OS}\theta_E}{\epsilon_{\text{th}} - 1} \right)^2. \quad (10)$$

3.2. The isothermal β model

Under the assumptions of spherical symmetry, isothermality, and the hydrostatic equilibrium for the ICM distribution, we can calculate the total gravitational mass within a radius r of a cluster whose ICM spatial distribution is described with the standard β model (Eq. 1):

$$M_{\text{cl}}^{\beta}(\leq r) = 3\beta \frac{k_{\text{B}}T_{\text{X}}}{G\mu m_p/r_c} \frac{(r/r_c)^3}{1 + (r/r_c)^2}, \quad (11)$$

where G is the gravitational constant, μ is the mean molecular weight, m_p is the proton mass, and r_c is a physical core radius; $r_c = D_{OL}\theta_c$, where D_{OL} is the angular diameter distance from the observer to the lens. We employ $\mu = 13/21$. Henceforth we call this model ‘isothermal β model’.

The density profile of the isothermal β model is given by

$$\rho(r) = \rho_0 \frac{(r/r_c)^2 + 3}{[1 + (r/r_c)^2]^2}; \quad \rho_0 \equiv \frac{3\beta}{4\pi} \frac{k_{\text{B}}T_{\text{X}}}{G\mu m_p/r_c} \frac{1}{r_c^3}. \quad (12)$$

The lens equation of the isothermal β model becomes

$$y = x - \mathcal{D} \frac{x}{[x^2 + 1]^{1/2}}, \quad (13)$$

where y [x] is the angle between the lens center and the source [the image] in the unit of θ_c , and \mathcal{D} is called the lens parameter:

$$\mathcal{D} \equiv \frac{6\pi\beta}{\theta_c} \frac{k_{\text{B}}T_{\text{X}}}{\mu m_p c^2} \frac{D_{LS}}{D_{OS}}. \quad (14)$$

When $\mathcal{D} \leq 1$, the lens always produces a single image of a source. On the other hand, the lens is able to form three images of a source when $\mathcal{D} > 1$.

Table 5. Central electron number density, cooling time, cooling radius and mass-flow rate of sample clusters.

Cluster name	n_{e0} [$10^{-3} h_{50}^{1/2} \text{cm}^{-3}$]		t_{cool} [Gyr]		t_{age} [$h_{50}^{-1} \text{Gyr}$]		θ_{cool} [arcsec]		\dot{M}_{cool} [$M_{\odot} \text{ yr}^{-1}$]	
	standard*	ENF98**	standard*	ENF98**	standard*	ENF98**	standard*	ENF98**	standard*	ENF98**
MS 0015.9+1609	7.2	6.9	13.9	14.5	11.4	0	0	0	0	0
MS 0302.7+1658	18.7	20.2	4.8	4.6	12.6	14	18	216	515	
MS 0353.6–3642	7.6	6.7	13.3	15.1	13.8	6	0	4	0	
MS 0451.5+0250	3.5	3.4	31.6	32.6	15.4	0	0	0	0	
MS 0735.6+7421	40.3	13.3	2.5	7.6	15.2	29	35	371	382	
MS 1006.0+1202	4.0	4.3	22.2	20.7	15.1	0	0	0	0	
MS 1008.1–1224	6.8	5.7	14.0	16.8	14.1	3	0	0.4	0	
MS 1224.7+2007	24.6	17.7	3.0	4.1	13.7	18	24	186	397	
MS 1333.3+1725	
MS 1358.4+6245	31.7	10.4	2.8	8.7	13.7	21	23	348	258	
MS 1455.0–2232	52.5	42.2	1.6	2.0	14.6	37	38	1732	1887	
MS 1512.4+3647	26.2	21.6	2.6	3.1	13.2	22	26	475	673	
MS 1621.5+2640	4.2	5.5	27.8	21.2	12.6	0	0	0	0	
MS 1910.5+6736	6.3	5.6	12.6	14.1	14.8	12	8	12	3	
MS 2053.7–0449	
MS 2137.3–2353	75.0	61.3	1.0	1.2	13.9	33	33	2253	2549	

* From standard β model (See Sec. 2.3) fitting results.

** From ENF98 β model (See Sec. 3.3) fitting results.

The moduli of the eigenvalues of the Jacobian matrix of the lens mapping are

$$\lambda_t(\text{tangential}) = \left| 1 - \frac{\mathcal{D}}{[x^2 + 1]^{1/2}} \right|, \quad (15)$$

$$\lambda_r(\text{radial}) = \left| 1 - \frac{\mathcal{D}}{[x^2 + 1]^{3/2}} \right|, \quad (16)$$

and the length-to-width ratio of an arc is

$$R_t(\text{tangential arc}) \equiv \frac{\lambda_r}{\lambda_t} = \left| \frac{1 - \mathcal{D}[x^2 + 1]^{-3/2}}{1 - \mathcal{D}[x^2 + 1]^{-1/2}} \right|, \quad (17)$$

or

$$R_r(\text{radial arc}) \equiv \frac{\lambda_t}{\lambda_r} = \left| \frac{1 - \mathcal{D}[x^2 + 1]^{-1/2}}{1 - \mathcal{D}[x^2 + 1]^{-3/2}} \right|. \quad (18)$$

3.3. The universal dark matter halo profile model

NFW made series of studies on the density profiles of dark matter halos formed through a gravitational collapse in hierarchically clustering cold dark matter (CDM) cosmology using N-body simulations. They concluded that dark matter halo reached a density profiles with a universal shape that did not depend on their mass ranging from dwarf galaxy halos to those of rich clusters, nor on the power spectrum of initial fluctuations, nor on the cosmological parameters through dissipationless hierarchical clustering. They found that the universal density profile can be spec-

ified by giving two parameters: the halo mass and the halo characteristic (dimensionless) density δ_c :

$$\frac{\rho_{\text{NFW}}(r)}{\rho_{\text{crit}}} = \frac{\delta_c}{(r/r_s)[1 + (r/r_s)]^2}, \quad (19)$$

where r_s is a scale radius related to the virial mass of the halo, and ρ_{crit} is the critical density:

$$\rho_{\text{crit}}(z) = \frac{3H(z)^2}{8\pi G} = \frac{3H_0^2}{8\pi G} [\Omega_{m0}(1+z)^3 + \Omega_{\Lambda0}], \quad (20)$$

for $\Omega_{m0} + \Omega_{\Lambda0} = 1$ cosmology.

The universal dark halo profile becomes one parameter function in the spherical top-hat model (e.g. ENF98). The virial mass M_{vir} is defined to be the mass contained within the radius, r_{vir} , that enclose a density contrast $\Delta_c : M_{\text{vir}} = (4\Delta_c\pi/3)\rho_{\text{crit}}r_{\text{vir}}^3$. This density contrast depends on the value of Ω and can be approximated by

$$\Delta_c(\Omega, z) = 178 \Omega(z)^{0.45}, \quad (21)$$

where

$$\Omega(z) = \frac{\Omega_{m0}(1+z)^3}{\Omega_{m0}(1+z)^3 + \Omega_{\Lambda0}}, \quad (22)$$

for $\Omega_{m0} + \Omega_{\Lambda0} = 1$ cosmology. This definition shows that the ratio of virial radius to scale radius, which is denoted by the ‘concentration’ parameter: $\mathcal{C} = r_{\text{vir}}/r_s$, uniquely related to δ_c by

$$\delta_c = \frac{\Delta_c}{3} \frac{\mathcal{C}^3}{\ln(1+\mathcal{C}) - \mathcal{C}/(1+\mathcal{C})}. \quad (23)$$

Table 6. Parameters of ENF98-NFW (and MSS98-NFW*) model.

Cluster name	δ_c [$\rho_{\text{crit}}(z)$]		r_s [h_{50}^{-1} Mpc]		r_{vir} [h_{50}^{-1} Mpc]		M_{vir} [$10^{14} h_{50}^{-1} M_\odot$]		T_{vir} [keV]
	ENF98	MSS98*	ENF98	MSS98*	ENF98	MSS98*	ENF98	MSS98*	ENF98
MS 0015.9+1609	6407	1041	1.14	1.74	5.78	3.77	145	35	34.9
MS 0302.7+1658	21606	9934	0.315	0.400	2.73	2.50	13	8.9	6.5
MS 0353.6–3642	8094	2514	0.787	0.945	4.60	3.28	51	16	15.5
MS 0451.5+0250	4676	516	1.67	2.67	7.92	4.40	214	37	37.6
MS 0735.6+7421	18019	53857	0.509	0.191	4.28	1.61	35	5.5	11.3
MS 1006.0+1202	5795	804	0.935	1.88	4.85	3.88	51	28	14.5
MS 1008.1–1224	7035	1148	0.861	1.04	4.76	2.49	55	8.1	16.0
MS 1224.7+2007	60568	33733	0.315	0.200	4.23	2.12	14	5.1	4.6
MS 1333.3+1725
MS 1358.4+6245	12451	23779	0.599	0.218	4.20	2.00	40	3.9	13.1
MS 1455.0+2232	54564	11405	0.270	0.314	3.53	2.13	21	5.2	8.2
MS 1512.4+3647	24594	9266	0.294	0.309	2.72	1.89	11	4.1	5.9
MS 1621.5+2640
MS 1910.5+6736	7345	3146	0.546	0.714	3.12	2.80	14	10	6.3
MS 2053.7–0449
MS 2137.3–2353	74641	20589	0.217	0.245	3.18	2.13	17	5.0	7.3

* See Sec. 5.

The structure of a halo mass M_{vir} is hence completely specified by a single parameter. The lens equation of the universal dark matter halo profile model is described as (Bartelmann 1996)

$$y = x - \mathcal{K} \frac{f(x)}{x}, \quad (24)$$

where y (x) is the angle between the lens center and a source (an image) in the unit of the angular scale radius (r_s/D_{OL}), \mathcal{K} is a constant coefficient:

$$\mathcal{K} \equiv 16\pi \frac{G}{c^2} \rho_{\text{crit}} \delta_c r_s \frac{D_{OL} D_{LS}}{D_{OS}}, \quad (25)$$

and

$$f(x) = \begin{cases} \ln \frac{x}{2} + \frac{2}{\sqrt{1-x^2}} \operatorname{arctanh} \sqrt{\frac{1-x}{1+x}} & (x < 1) \\ 1 - \ln 2 & (x = 1) \\ \ln \frac{x}{2} + \frac{2}{\sqrt{x^2-1}} \operatorname{arctan} \sqrt{\frac{x-1}{x+1}}; & (x > 1). \end{cases} \quad (26)$$

ENF98 performed cosmological hydrodynamical and particle simulations to examine the evolution of X-ray emitting hot gas in clusters in a flat ($\Omega_{m0} + \Omega_{\Lambda0} = 1$), low-density ($\Omega_{m0} = 0.3$) CDM cosmology. They showed that radial density profiles of gas in relaxed clusters are well described by the standard β model. Table 3 in ENF98 enables us to calculate δ_c and r_s from the X-ray data. They have shown that the β values of most of their simulated clusters are around 0.79 if we exclude the cluster which is

likely in dynamically non-equilibrium state. Parameters of the universal density profile is thereby specified with the observed core radius r_c and the normalized central gas densities δ_{gas} using the relations of

$$r_s = 2.65r_c$$

and

$$\delta_c = 3.99\delta_{\text{gas}}$$

found in their result for $\beta_{\text{fit}} = 0.79$. In applying this model to our data, we had to remind that the best-fit β value got artificially lower as the central surface brightness got closer to the background surface brightness (e.g. Bartelmann & Steinmetz 1996). In general, the central surface brightnesses of high redshift clusters are very low and close to the background of ROSAT HRI. It is hence likely that the best-fit values of β shown in Table 2 are biased by this effect. To overcome this problem, we employed another β model (henceforth ‘ENF98 β model’) fitting in which β was fixed to the median value of β in Table 3 of ENF98; $\langle \beta_{\text{fit}} \rangle_{\text{median}} = 0.79$. In this procedure, we implicitly assumed that if the radial profile was resolved up to the virial radius, the β should be ~ 0.79 . We list the ENF98 β model fitting result in Table 3. We also list fluxes, luminosities and temperatures of the sample clusters calculated using the best-fit values of the ENF98 β model fitting on the right hand side of each column in Table 4. We also list central electron number densities, central cooling times, ages of the universe at the redshift of each cluster, cooling radii, and mass-flow rates (\dot{M}_{cool}) for the sample clusters on the right hand side in each column in Table 5. On the

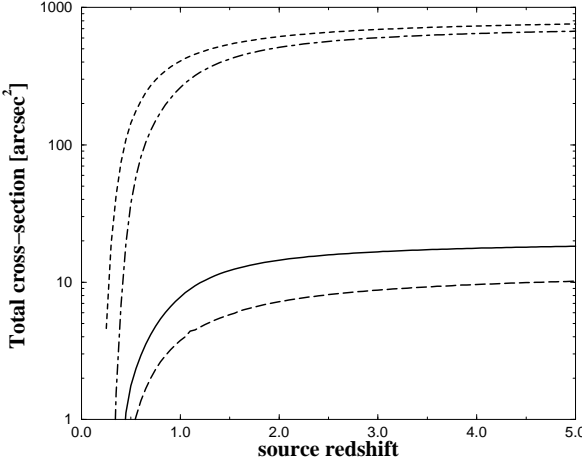


Fig. 1. Total cross-section against source redshift. The total cross-section is calculated by summing up all the cross-section of each sample cluster. A cross-section for a sample cluster to make giant arcs of background galaxies with a lens model is an area on the source plane in which background circular galaxies show their images with length-to-width ratio greater than or equal to 10 in the image plane. Clusters MS 1333.3+1725, MS 1621.5+2640, and MS 2053.7-0449 are excluded in the calculation with isothermal β model, ENF98-NFW model, and MSS98-NFW model (See Sec. 5). Dashed line: the SIS model. Solid line: the isothermal β model. Dot-dashed line: the ENF98-NFW model. Long-dashed line: the MSS98-NFW model (See Sec. 5).

left hand side of each column in Table 6, we list values of parameters of the NFW model (henceforth *ENF98-NFW model*) derived from *ROSAT HRI* data using the procedure described above. The virial mass was evaluated using the equation (Makino et al. 1998)

$$M_{\text{vir}} = 4\pi\delta_c\rho_{\text{crit}}r_s^3 \left[\ln(1 + \mathcal{C}) + \frac{\mathcal{C}}{1 + \mathcal{C}} \right]. \quad (27)$$

For the ENF98-NFW model, one can evaluate its virial temperature T_{vir} :

$$k_B T_{\text{vir}} = \frac{1}{2}\mu m_p \frac{GM_{\text{vir}}}{r_{\text{vir}}} \quad (28)$$

using *only* the information of ICM spatial distribution; β and θ_c . Some clusters have virial temperatures which are much higher than temperatures obtained by *ASCA* or obtained using the $L_X - T$ relation of AE98.

3.4. Total cross-sections to make giant arcs

In Fig. 1, we show total cross-sections of LF94 sample to make giant arcs of background galaxies assuming that

the background source galaxies are circular. Dashed line, solid line, dot-dashed line, and long-dashed line respectively represent the total-cross section to make giant arcs calculated with the SIS model, the isothermal β model, the ENF98-NFW model, and the MSS98-NFW model (we discuss this model in Sec. 5). A cross-section of a sample cluster to make giant arcs of background galaxies with a lens model is an area on the source plane in which background galaxies show their images with length-to-width ratio greater than or equal to 10 in the image plane. The total cross-section is calculated by summing up all the cross-sections of sample clusters. We calculated the total cross-section with the SIS model using $\sigma - T$ relation used in HF97. Note that clusters MS 1333.3+1725, MS 1621.5+2640, and MS 2053.7-0449 are excluded in the calculation with the isothermal β model, the ENF98-NFW model, and MSS98-NFW model (See Sec. 4.3). As shown in Fig. 1, the total cross-sections calculated with the ENF98-NFW model and that with the SIS model are comparable for all the source redshifts. Considerably larger total cross-section of the ENF98-NFW model than that of the isothermal β model is due to their much higher T_{vir} . The main reason why HF97 could reproduce the observed number of GLAs in the LF94 sample is considerably high temperatures which they overestimated with inappropriate $L_X - \sigma$ relation.

3.5. Properties of the giant luminous arcs

In Table 7, observational properties of GLAs found in the LF94 sample are summarized as follows; major axis length: l , length-to-width ratio: l/w , distance from the cluster center: d , apparent magnitude: m , the projected mass within Einstein ring radii θ_E regarding $d = \theta_E$:

$$M_{\text{GLA}}^{\text{Einstein}}(\theta_E) = \frac{c^2}{4\pi G} \frac{D_{\text{OS}}}{D_{\text{OL}} D_{\text{LS}}} \pi (D_{\text{OL}} \theta_E)^2,$$

the projected mass deduced from the isothermal β model:

$$M_{\text{X}}^{\text{IT}\beta}(\theta_E) = \frac{3\pi\beta}{2} \frac{k_B T_{\text{X}}}{G\mu m_p/r_c} \frac{(\theta_E/\theta_c)^2}{[1 + (\theta_E/\theta_c)^2]^{1/2}},$$

and the projected mass deduced from the ENF98-NFW model:

$$M_{\text{X}}^{\text{NFW}}(\theta_E) = 4\pi\rho_{\text{crit}}\delta_c r_s^3 f(x_E),$$

where $x_E = D_{\text{OL}}\theta_E/r_s$, assuming source redshift $z_s = 1$.

4. The statistics of giant luminous arcs

In this section, we examine the expected numbers of GLAs predicted by the isothermal β model and the ENF98-NFW model using the numerical code described in detail in Paper I.

4.1. The theoretical model of galaxy evolution

As is in Paper I, prescriptions of properties of background galaxies are essentially the same as those in Yoshii & Takahara (1988) and Yoshii & Peterson (1991). We adopted the galaxy type mixing ratio of (E/S0, Sab, Sbc, Scd, Sdm)=(0.215, 0.185, 0.160, 0.275, 0.165) given by Pence (1976). The K and E corrections for each type were calculated using the type-dependent, present day spectral energy distribution (SED) updated by Yoshii & Peterson (1991) and the type-dependent galaxy luminosity evolution models by Arimoto & Yoshii (1986 & 1987), except for the UV light of E/S0 galaxies. We adopted the UV-intermediate NGC3379 SED (henceforth ‘case I’) and the UV-bright NGC4649 SED (henceforth ‘case II’) as the SED for E/S0 galaxies. These models are reliable, especially at low redshift of $z < 1$ (Yoshii & Takahara 1988, Totani et al. 1997). Although recent observations of galaxies and their evolution at $z > 1$ (e.g. Roche et al. 1998 and references therein) have considerably been improving our knowledge of them, these models are still in good agreement with such recent observations; e.g. data of star formation history taken by the Hubble Space Telescope (Madau et al. 1996) or galaxy number counts (Yoshii & Peterson (1991)). We discuss some effects of the recent new knowledge for the galaxy evolution (e.g. a major merger of galaxies) on our GLA statistics bellow. The luminosity function of all galaxy types was assumed to be same and was taken from Efstathiou, Ellis & Peterson (1988), namely the Schechter function with $\alpha = -1.07$, $\phi_* = 1.56 \times 10^{-2} h^3 \text{Mpc}^{-3}$ and $M_B^* = -19.39 + 5\log h$ (h is the Hubble constant in the unit of $100 \text{km s}^{-1} \text{Mpc}^{-1}$). The galaxy formation epoch was assumed to be $z_F = 5$. The absolute magnitude in B band for each type of galaxies was converted into V band magnitude using the relation $M_V = M_B + (V - B)$ where $(V - B) = -1.03$ for E/S0, -0.79 for Sab, -0.64 for Sbc, -0.56 for Scd and -0.46 for Sdm. No evolution in the comoving galaxy number density was assumed for the galaxy luminosity function. The luminosity profiles and the effective radii for each galaxies were modeled as the same way in Paper I. The intrinsic shape of the source galaxy image was assumed to be circular.

4.2. The detection condition and the arc identification scheme

The detection condition in the LF94 arc survey were taken into account as the same way in Paper I. The adopted GLA identification scheme was also same as described in section 2.4 of Paper I. The length-to-width condition and the apparent magnitude condition were applied for the images smeared by the seeing and by the limiting surface brightness. The threshold value for the axis ratio and the apparent V magnitude respectively were set to be $\epsilon_{\text{th}} = 10$ and $m_V(\text{arc}) = 22.5$.

4.3. Numbers of giant luminous arcs

As noted above, the object MS 1333.3+1725 is not a cluster and thus was excluded from the cluster sample. Since the central surface brightness of cluster MS 1621.5+2640 is very close to the background, X-ray emission from only the central small portion was resolved by *HRI* (Morris et al. 1998). Because of this reason and poor photon statistics, the standard β model fitting gave unusual values as the best-fit result and it was impossible to estimate its errors. The ENF98 β model fitting for this cluster did not converge. The cluster MS 1621.5+2640 in which a GLA is found hence was excluded from the arc statistics sample in the current studies, following which the observed number of GLAs in the sample of 14 clusters becomes 5. Although two giant arcs were detected by the Hubble Space Telescope in clusters MS 1358.4+6245 (Franx et al. 1997) and MS 1512.4+3647 (Seitz et al. 1997), they are not extremely bright and hence do not enter the GLA statistics. X-ray emission from object MS 2053.7–0449 was not detected in spite of pointing observation with 5 ksec exposure time. The 3σ upper limit on the X-ray flux of MS 2053.7–0449 was set. The upper limit on the temperature could be obtained from this upper limit by following procedure. First the temperature was assumed to be 6 keV and the upper limit of X-ray luminosity was calculated. Then using the $L_X - T$ relation, the temperature value was reset and an upper limit of X-ray luminosity was recalculated with this temperature. Iterating this procedure until the value of the temperature converged, the upper limit on temperature listed in Table 4 was obtained. The β value of MS2053.7–0449 was assumed to be 2/3. A core radius of 10 arcsec for MS2053.7–0449 was also assumed because smaller core radius makes a cluster more efficient to make GLAs. Unfortunately, we could not calculate the central electron number density of MS2053.7–0449 and therefore MS2053.7–0449 was excluded from the GLA statistics with the ENF98-NFW model (and with MSS98-NFW when we calculate total cross-section to make giant arcs). The expected number of GLAs hence becomes 4/13 in this case. The expected numbers of GLAs in LF94 sample, N_{arc} , were calculated summing up all the expected numbers of GLAs in each cluster, $N_{i,\text{arc}}$, which were described in detail in Paper I.

We list the result in Table 8. It shows that the isothermal β model consistent with current best X-ray data, cannot reproduce the observed large number of GLAs in the LF94’s sample. On the other hand, the ENF98-NFW model marginally reproduces the observed number of GLAs in the LF94 sample. However, as one can see in Table 6, some clusters have extraordinary high T_{vir} which are in disagreement with the temperatures measured by *ASCA* or estimated using the $L_X - T$ relation of AE98. The dominant contribution to increasing the predicted number of GLAs is these high temperature clusters.

Table 7. Properties of the giant luminous arcs from TABLE 1 in LF94.

Cluster name	l [arcsec]	l/w	d [arcsec]	m [magnitude]	$M_{\text{GLA}}^{\text{Einstein}}$ [$10^{14} M_{\odot}$]	$M_{\text{X}}^{\text{IT}\beta}$ [$10^{14} M_{\odot}$]	$M_{\text{X}}^{\text{NFW}}$ [$10^{14} M_{\odot}$]
MS 1006.0+1202	5.9	10.5	26	$V = 21.92$	1.2	0.37	7.3
MS 1008.1–1224	4.5	10	47	$V = 21.53$	5.5	1.8	4.3
MS 1621.5+2640	9.8	19.6	16 *	$V = 21.16$	1.0	3.4	...
MS 1910.5+6736	6.1	10.5	67	$V = 22.29$	8.7	1.8	4.0
MS 2053.7–0449	10.5	17.5	15.8	$R = 21.91$
MS 2137.3–2353	14.2	17.8	15.5	$V = 22.0$	0.62	0.41	1.1

* From the second brightest cluster member galaxy. For further details, see Luppino & Gioia (1992) and Ellingson et al. (1997).

Table 8. Expected number of giant luminous arcs. Case I: E/S0 SED is UV-intermediate NGC3379 SED. Case II: E/S0 SED is UV-bright NGC4649 SED.

Model	Case I	Case II	observed number
Isothermal β model	0.031	0.055	5*
ENF98-NFW model	1.7	3.8	4*

* See Sec. 4.3.

5. Discussion

Although the ENF98-NFW model could marginally reproduce the observed number of GLAs in the LF94's sample, some clusters have unrealistic T_{vir} . If ENF98-NFW model describes the truth and if it is this high virial temperature that describes the true depth of gravitational potential of clusters, the non-thermal pressure model (Loeb & Mao 1994) or the cooling flow model (Allen 1998) would be expected. However, as shown in Table 5, cooling times of *all* the clusters with $T_{\text{vir}} > 14$ keV are longer than the ages of the universe at clusters' redshifts. This indicates that higher T_{vir} obtained from the ENF98 β model fitting were not due to the existence of cooling flows. The high values of T_{vir} are likely due to too large values of the scale radii r_s . The large values of scale radii (r_s) come from large X-ray core radii (r_c) and those who have large X-ray core radii show significant ellipticity. As NFW discussed, their profile came from the virialized system and those which have too high T_{vir} hence would be regarded as in relaxing process.

For the comparison, we calculated a total cross-section to make giant arcs with another NFW type model in which temperatures are required to be those that are observed by ASCA or that are estimated using $L_{\text{X}} - T$ relation of AE98 using the result of a theoretical work by Makino et al. (1998, henceforth MSS98). MSS98 computed the X-ray cluster gas density distribution in hydrostatic equilibrium from NFW model assuming isothermality of the ICM. MSS98 showed that the resulting distribution was well approximated by the standard β model. Their result

gives relations of

$$r_s = r_c / 0.22 \sim 4.55 r_c,$$

$$\beta = 0.9b,$$

and

$$b = \frac{8\pi G \mu m_p \delta_c \rho_{\text{crit}} r_s^2}{27 k_B T_{\text{X}}},$$

and we could evaluate δ_c and r_s (henceforth we call this model *MSS98-NFW model*). We list the parameters of MSS98-NFW in Table 6 and we plotted the total cross-section to make giant arcs with MSS98-NFW model with long-dashed line in Fig. 1. As one can see in Fig. 1, the total cross-section to make giant arcs is considerably small and almost the same as the isothermal β model. This means the NFW model which is consistent with the ICM spatial and spectral data of sample clusters cannot reproduce the observed number of GLAs.

This is also the same to say that what is needed is just to make the sample clusters' temperatures much higher to reproduce the observed number of GLAs. However, such high temperatures are no more consistent with ASCA results or expected values from the $L_{\text{X}} - T$ relation of AE98.

Systematic errors introduced by uncertainties in the background galaxy model we employed are summarized as follows.

As is in Paper I, the luminosity function was taken from Efstathiou et al. (1988). This luminosity function is in good agreement with the recent Las Campanas (Lin et

al. 1996) and the Stromro-APM (Loveday et al. 1992) redshift surveys. These are called luminosity functions with lower normalization. On the other hand, the ESO Slice Project redshift survey (Zucca et al. 1997) gives higher normalization. Its amplitude is then higher, by a factor of ~ 1.6 at $M \sim M^*$. Luminosity functions with higher normalization thereby increase the number of GLAs, with rough estimation, by a factor of two. As noted above, we assumed no evolution of galaxy number density in the comoving volume for the luminosity function. On the other hand, HF97 showed that observed evolution of the luminosity function, which came from Canada France Redshift Survey (Lilly et al. 1995), increases the number of GLAs by a factor of several.

We investigated whether changing the type mixing ratio of background galaxies affected the GLA number by changing (E/S0, Sab, Sbc, Scd, Sdm)= (0.321, 0.281, 0.291, 0.045, 0.062) and (0.38, 0.16, 0.25, 0.10, 0.11) and then little difference was found.

As is in Paper I, the amplification factor was approximately constant over the whole area of an image and the validity of this assumption has already been confirmed in Paper I.

The intrinsic ellipticity of source galaxies could increase the number of GLAs by a factor of two as discussed in Paper I.

All these may affect on the expected number of GLAs by about an order of magnitude at most. Therefore even if uncertainties in the background galaxy model are taking into account, the main conclusion never change; the models consistent with the ICM spatial and spectral data of sample clusters, cannot reproduce the observed number of GLAs in the LF94's sample.

As noted in Sec. 4, recent observations give us new insights on galaxy surface brightness and size evolution up to $z \sim 4$ (Roche et al. 1998 and references therein). There is no size and luminosity evolution of elliptical galaxies at higher redshift (Roche et al. 1998). Spiral galaxies become smaller in size and brighter in surface brightness as redshift increases (Roche et al. 1998). Miralda-Escudé (1993b) and Paper I showed that the number of GLAs responds sensitively on the intrinsic size of galaxies and the number of GLAs decreases drastically when the intrinsic size of galaxies becomes smaller than the seeing FWHM. (See Fig. 3 in Miralda-Escudé 1993b or Fig. 4 in Paper I). We believe that this effect is stronger than that of surface brightness evolution because spirals seems not showing strong evolution in luminosity.

If the galaxy evolution history is drawn with the merger model which is currently popular (e.g. Kauffmann 1997; Bekki 1997; Bekki & Shioya 1997; Noguchi 1997), the galaxy evolution model we employed should be largely modified. Owing to merging-induced star formation, the merger model predicts the existence of temporarily very

bright galaxies at various redshifts. Since the current galaxies are to be formed by aggregation of smaller building blocks in the merger model, the number density of source galaxies at high redshift is larger than the current galaxy number density. These two effects may thus increase the number of GLAs. Although the precise modeling of the merger history is required to quantify the effect, we can regard that these effects are included as re-normalization in the evolution of the galaxy luminosity function. The result obtained by HF97 thus provided a rough idea how this effect changes model prediction. On the other hand, as we discussed above, smaller size of the block-building galaxies at high redshift leads drastic decrease of the number of GLAs. Becoming larger in size by merging is competed by becoming less in number of galaxies by merging. On the arc statistics, the effect of being smaller intrinsically seems stronger than both being more luminous intrinsically and being numerous at high redshift.

Asada (1998) showed that the use of the Deyer-Roeder distance to take into account the inhomogeneity of matter distribution in the universe decreased the cross-section for forming GLAs for all the sets of (Ω, Λ, H) . Therefore the appropriate application of angular diameter distance taking account of the inhomogeneity of the universe further decrease the number of GLAs.

Our calculation assumed that one GLA is generated from one single source galaxy. However, it may happen that two or more GLAs are generated from a single source galaxy. This means that the '*true*' expected numbers of GLAs exists between one times the expected numbers we calculated and two times of them under the spherically symmetric mass distribution models.

We close our discussion by this simple question: are *all* observed GLAs in LF94's sample *really* giant luminous arcs? LF94 discussed the possibility of mis-identification by elongated objects and claimed that 6 GLAs they found were really GLAs either because their widths were not spatially resolved, or because they presented a well-defined curvature. However, the giant luminous arcs in MS 1910.5+6736 and MS1008.1-1224 are located 67 and 47 arcsec away from cluster center respectively, which are unusually large values that would make the cluster extremely massive. Although, such mis-identification does not affect our result, it would seriously affect the GLA statistics which use the number of GLA on the whole sky extrapolating the GLA detecting rate in EMSS sample. Spectroscopic conformation of GLAs therefore is needed for all the GLAs in the sample.

6. Conclusions

We studied the statistics of GLAs with spherically symmetric lens models based on our original X-ray spatial data of all the 15 clusters in the LF94's arc survey sample, obtained by *ROSAT HRI*. We re-investigated whether the observed number of GLAs in the LF94's cluster sample could be reproduced with the cluster mass distribution models consistent with the X-ray data of spatial distribution of the ICM within a frame work of spherical symmetry assuming isothermality and the hydrodynamical equilibrium. We employed two types of cluster mass distribution models. One is a model comes from the conventional β model used for X-ray spatial data fittings (the 'isothermal beta model' in this paper). The other is the universal dark matter halo profile model proposed by NFW (the 'ENF98-NFW model' and the 'MSS98-NFW model' in this paper). The ENF98-NFW model is a model with the result of cosmological and hydrodynamical simulations to examine the evolution of X-ray emitting hot gas in clusters, by ENF98. The MSS98-NFW model is a model with the result of the theoretical work by MSS98. Models consistent with current best data of spatial distribution of the ICM in the sample clusters taken by *ROSAT HRI* (isothermal beta model and MSS98-NFW model) gave the numbers of GLAs less than two orders of magnitude and this fewness is significant comparing to the uncertainties in the background galaxy model we employed. On the other hand, ENF98-NFW model almost reproduced the observed number of GLAs. Some clusters' virial temperatures of this model, however, are much higher than the temperatures measured by *ASCA* or evaluated from the $L_X - T$ relation of AE98. This indicates that either: non-thermal components of the pressure play a significant role in supporting the ICM (e.g. Loeb & Mao 1994) or the mass distribution of sample clusters deviates significantly from the spherical symmetry. For example, MS1006.0+1202 has straight arcs which cannot be formed by spherically symmetric mass distribution. Some sample clusters show significant irregularity in their X-ray morphologies. We believe that taking into account the irregularity in mass distribution of clusters is therefore very important subject and will constitute the next step together with a better handling of the temperature measurement of the ICM.

Acknowledgements. KM and MH would like to thank Toshi-fumi Futamase and Takashi Hamana for insightful comments. JPK thanks the Astronomical Institute of Tohoku University and Yamada Science Foundation for fruitful visit to Japan. This work was supported by the Sasakawa Scientific Research Grant from the Japan Scientific Society (10-099). MH is supported by Yamada Science Foundation and by the Grants-in-Aid by the Ministry of Education, Science and Culture of Japan (09740169, 60010500).

Appendix.

We note down individual clusters with overlays of significance contour plots superposed on the Digitized Sky Survey⁴ optical images and radial profiles. A significance contour plot is made from an X-ray image smoothed with a Gaussian filter with a σ of $15''$ after subtracting the background. The lowest contour levels is 2σ . In each radial profile, the solid line and the dashed line respectively represent the result of fitting with standard β model and ENF98 β model. The dotted line represents the point spread function at the position of each X-ray center.

MS 0015.9+1609 (Cl 0016+16)

One correlation was found between the brightest point source in the *HRI* field of view and objects cataloged in ROSID: QSO0015+162. As Neumann & Böhringer(1997, henceforth NB97) mentioned, there are two observations for this cluster. Each exposure time was 70 ksec and 2 ksec. NB97 merged two observational data referring the position of the QSO. However, since 1)there is only one source available for the pointing check of 2 dimensional position and 2) 70 ksec exposure time is long enough compared with $70+2 = 72$ ksec exposure time, we used only the data of 70 ksec exposure time to avoid systematic error which comes from merging 2 dimensional data referring only one source position. Our result of standard β model fitting to *HRI* data is slightly different from NB97's result of the β model fitting to *HRI* data (but consistent with it within 90 % errors) and rather consistent with their results of that of PSPC data. The position of QSO0015+162 on *HRI* is

⁴ The Digitized Sky Surveys were produced at the Space Telescope Science Institute under U.S. Government grant NAGW-2166. The images of these surveys are based on photographic data obtained using the Oschin Schmidt Telescope on Palomar Mountain and the UK Schmidt Telescope. The plates were processed into the present compressed digital form with the permission of these institutions.

The National Geographic Society – Palomar Observatory Sky Atlas (POSS-I) was made by the California Institute of Technology with grants from the National Geographic Society.

The Second Palomar Observatory Sky Survey (POSS-II) was made by the California Institute of Technology with funds from the National Science Foundation, the National Geographic Society, the Sloan Foundation, the Samuel Oschin Foundation, and the Eastman Kodak Corporation.

The Oschin Schmidt Telescope is operated by the California Institute of Technology and Palomar Observatory.

The UK Schmidt Telescope was operated by the Royal Observatory Edinburgh, with funding from the UK Science and Engineering Research Council (later the UK Particle Physics and Astronomy Research Council), until 1988 June, and thenceforth by the Anglo-Australian Observatory. The blue plates of the southern Sky Atlas and its Equatorial Extension (together known as the SERC-J), as well as the Equatorial Red (ER), and the Second Epoch [red] Survey (SES) were all taken with the UK Schmidt.

($00^{\text{h}}18^{\text{m}}32^{\text{s}}15$, $+16^{\text{d}}29^{\text{m}}25^{\text{s}}5$)(J2000). The position of X-ray center on *HRI* is ($00^{\text{h}}18^{\text{m}}33^{\text{s}}73$, $+16^{\text{d}}26^{\text{m}}07^{\text{s}}5$)(J2000)

MS 0302.7+1658 (Cl 0302+1658)

One observation was performed for this cluster. No correlation was found between sources higher than 3σ in the *HRI* field of view and objects cataloged in HRASSCAT or ROSID. The position of the X-ray center on *HRI* is ($03^{\text{h}}05^{\text{m}}31^{\text{s}}94$, $+17^{\text{d}}10^{\text{m}}05^{\text{s}}0$)(J2000). The position of the X-ray peak is consistent with that of the brightest cluster member galaxy within the *HRI* pointing accuracy.

MS 0353.6–3642 (S 400)

One observation was performed for this cluster. No correlation was found between sources higher than 3σ in the *HRI* field of view and objects cataloged in HRASSCAT or ROSID. This cluster does not show a significant X-ray peak, i.e. the X-ray center, we therefore defined the X-ray center as source count rate weighted mean position of sources around pointing center. The source count rates are calculated by the EXSAS command “DETECT/SOURCES”.

MS 0451.5+0250 (Abel 520)

One observation was performed for this cluster. No correlation was found between the sources higher than 3σ in the *HRI* field of view and objects cataloged in HRASSCAT or ROSID. This cluster does not show a significant X-ray peak, i.e. the X-ray center, we therefore define the X-ray center as source count rate weighted mean position of sources around pointing center. The source count rates were calculated by the EXSAS command “DETECT/SOURCES”.

MS 0735.6+7421 (ZwCl 0735.7+7421)

One observation was performed for this cluster. No correlation was found between sources higher than 3σ in the *HRI* field of view and objects cataloged in HRASSCAT or ROSID. The position of the X-ray center is consistent with that of the brightest cluster member galaxy within the *HRI* pointing accuracy.

MS 1006.0+1202 (ZwCl 1006.1+1201)

Three observations were performed for this cluster. Each exposure time was 3 ksec, 20 ksec, and 65 ksec. No correlation was found between sources higher than 3σ in the *HRI* field of view and objects cataloged in HRASSCAT or ROSID. We used only the data of 65 ksec exposure time to avoid systematic error in merging the data without any references because 65 ksec exposure seemed long enough. This cluster does not show a significant X-ray peak, i.e.

the X-ray center, we therefore defined the X-ray center as source count rate weighted mean position of sources around pointing center. The source count rates were calculated by the EXSAS command “DETECT/SOURCES”.

MS 1008.1–1224

One observation was performed for this cluster. No correlation was found between sources higher than 3σ in the *HRI* field of view and objects cataloged in HRASSCAT or ROSID. X-ray center (J2000.0) is ($10^{\text{h}}10^{\text{m}}32^{\text{s}}42$, $-12^{\text{d}}39^{\text{m}}47^{\text{s}}0$).

MS 1224.7+2007

Four observations were performed for this cluster. Each exposure time was 14 ksec, 24 ksec, 5 ksec, and 13 ksec. No correlation was found between sources higher than 3σ in the *HRI* field of view and objects cataloged in both HRASSCAT and ROSID. One, and the only one, cataloged bright point source was available for comparison of pointing accuracy in each image. We therefore used only the data of 24 ksec exposure time which was the longest one among them, to avoid systematic error which came from merging data referring only one source position. X-ray center (J2000.0) is ($12^{\text{h}}27^{\text{m}}13^{\text{s}}28$, $+19^{\text{d}}50^{\text{m}}57^{\text{s}}0$).

MS 1333.3+1725

One observation was performed for this cluster. One correlation was found between sources higher than 3σ in the *HRI* field of view and objects cataloged in HRASSCAT and ROSID: QSO1333+177.

As the contour plot and the radial profile show, this object is not a cluster but an X-ray point source. Therefore this object was excluded from the sample.

MS 1358.4+6245 (ZwCl 1358.1+6245)

Two observations were performed for this cluster. Each exposure time was 14 ksec and 16 ksec. One correlation was found between sources higher than 3σ in the *HRI* field of view and objects cataloged in HRASSCAT: J135903.4+621239. However, J135903.4+621239 locates near the edge of *HRI* field of view and was not usable for the reference of the pointing accuracy check. There was also a bright source not cataloged and thus only one point source near the pointing center available for the reference of the pointing accuracy check. Since the exposure times of two observations were comparable to each other and each exposure time is not long enough, we chose the way to merge two files believing that pointing of each observation is completely identical. The difference of position of the point source near the pointing center is $3''$ in RA and $2''$ in DEC and therefore we can say that these two positions are identical within the *HRI* pointing accu-

racy. Position of the X-ray center on *HRI* is ($13^{\text{h}}59^{\text{m}}50\overset{\text{s}}{.}34$, $+62^{\text{d}}31^{\text{m}}04\overset{\text{s}}{.}5$)(J2000). The position of the X-ray center is consistent with that of the brightest cluster member galaxy within the *HRI* pointing accuracy.

MS 1455.0–2232 (1E 1455+2232)

Three observations were performed for this cluster. Each exposure time was 4 ksec, 4 ksec, and 7 ksec. No correlation was found between sources higher than 3σ in the *HRI* field of view and objects cataloged in HRASSCAT or ROSID. Since the exposure times of three observations were comparable to each other and each exposure time is not long enough, we chose the way to merge three files believing that the pointing of each observation was completely identical. The position of the X-ray center on *HRI* is ($14^{\text{h}}57^{\text{m}}14\overset{\text{s}}{.}94$, $+22^{\text{d}}20^{\text{m}}35\overset{\text{s}}{.}5$)(J2000). The position of the X-ray center is consistent with that of the brightest cluster member galaxy within the *HRI* pointing accuracy.

MS 1512.4+3647

One observation was performed for this cluster. Two correlations were found between sources higher than 3σ in the *HRI* field of view and objects cataloged in ROSID: QSO1512+370 and HD135657. The position of the X-ray center on *HRI* is ($15^{\text{h}}14^{\text{m}}22\overset{\text{s}}{.}65$, $+36^{\text{d}}36^{\text{m}}20\overset{\text{s}}{.}0$)(J2000). The position of the X-ray center is consistent with that of the brightest cluster member galaxy within the *HRI* pointing accuracy.

MS 1621.5+2640

One observation was performed for this cluster. No correlation was found between sources higher than 3σ in the *HRI* field of view and objects cataloged in HRASSCAT or ROSID. The *HRI* image of MS 1621.5+2640 shows double peaks and therefore we defined the X-ray center as the position of the second brightest cluster member galaxy. (First brightest cluster member galaxy locates about $3'$ away from X-ray center (Ellingson et al. 1997).) This position is near the center of double X-ray peaks. This cluster shows very poor signal-to-noise ratio. Forcing standard β model fitting gave unusual values for its best-fit (Morris et al. 1998). We also fit the PSPC data, which has the lower background than *HRI*, and only to give us unacceptable χ^2 value same as the case of *HRI*. PSPC data showed that the position where the tail of radial profile from *HRI* meets the background was still in the cluster source region on the PSPC image. Therefore β model fitting to *HRI* data is not applicable. This cluster is excluded from the arc statistics.

MS 1910.5+6736

One observation was performed for this cluster. No correlation was found between sources higher than 3σ in the

HRI field of view and objects cataloged in HRASSCAT or ROSID. The position of the X-ray center on *HRI* is ($19^{\text{h}}10^{\text{m}}27\overset{\text{s}}{.}94$, $+67^{\text{d}}41^{\text{m}}28\overset{\text{s}}{.}0$)(J2000).

MS 2053.7–0449

One observation was performed for this cluster. No correlation was found between sources higher than 3σ in the *HRI* field of view and objects cataloged in HRASSCAT or ROSID.

In spite of 5 ksec pointing, we could have no source photons of MS 2053.7–0449. This indicates the low signal-to-noise ratio of this cluster. We gave the upper limit of the central surface brightness assuming $\beta_{\text{fit}} = 2/3$ for analytical calculation. This cluster was excluded from our GLA statistics with the ENF98-NFW model and the MSS98-NFW model. For the GLA statistics with Isothermal β model, core radius was assumed to be $10''$.

MS 2137.3–2353

Two observations were performed for this cluster. Each exposure time was 2 ksec and 14 ksec. No correlation was found between sources higher than 3σ in the *HRI* field of view and objects cataloged in HRASSCAT or ROSID. Since 14 ksec exposure time is long enough comparing with $14 + 2 = 16$ ksec exposure time, we used only the data of 14 ksec exposure time to avoid systematic error which came from merging data with no references. The position of the X-ray center on *HRI* is ($21^{\text{h}}40^{\text{m}}15\overset{\text{s}}{.}17$, $-23^{\text{d}}39^{\text{m}}41\overset{\text{s}}{.}0$)(J2000). The position of the X-ray center is consistent with that of the brightest cluster member galaxy within the *HRI* pointing accuracy.

References

- Allen, S.W., 1998, MNRAS 296, 392
- Allen, S.W., Fabian, A.C., Kneib, J.-P., 1996, MNRAS 279, 615
- Arimoto, N., Yoshii, Y., 1986, A&A 164, 260
- Arimoto, N., Yoshii, Y., 1987, A&A 173, 23
- Arnaud, M., Evrard, A.E. 1998, MNRAS submitted.; astro-ph/9806353 (AE98)
- Asada, H. 1998, ApJ in press;astro-ph/9803004
- Bahcall, N.A., Lubin, R.M., 1994, ApJ, 426, 513
- Bartelmann, M., Weiss, A., 1994, A&A 287, 1
- Bartelmann, M., Steinmetz, M., Weiss, A. 1995, A&A 297, 1 (BSW95)
- Bartelmann, M., 1996, A&A 313, 697
- Bartelmann, M., Steinmetz M., 1996, MNRAS 283, 431
- Bartelmann, M., Huss, A., Colberg, J.M., Jenkins, A., Pearce, F.R., 1998, A & A, 330, 1
- Bekki, K., 1997, in *Galaxy Interactions at Low and High Redshift*, IAU Symposium 186
- Bekki, K., Shioya, Y., 1998, ApJL 478, L17
- Bézecourt, J., Pelló, R., Soucail, G., A&A 330, 399
- Böhringer, H., Tanaka, Y., Mushotzky, R.F., Ikebe, Y., Hattori, M., 1998, A&A 334, 789

- Cavaliere, A., Fusco-Femiano, R., 1976, A&A, 49, 137
- David, L.P., Slyz, A., Jones, C., Forman, W., Virtle, S., Arnaud, K., 1993, ApJ, 412, 479
- Dickey, J.M., Lockman, F.J. 1990, ARA&A, 28, 215
- Efstathiou, G., Ellis, R.S., Peterson, B.A., 1988, MNRAS 232, 431
- Eke, V.R., Navarro, J.F., Frenk, C.S., 1998, ApJ 503, 569
- Ellingson, E., Yee, H.K.E., Abraham, R.G., Morris, S.L., Carlberg, R.G., Smecker-Hane, T.A., 1997, ApJS 113, 1
- Ellis, R., 1998, in *Cosmological Parameters & Evolution of the Universe*, ed Sato, K., IAU Symposium 183
- Fabian, A.C., 1994, ARA&A 32, 277
- Fort, B., Mellier, Y., 1994, A&AR 5, 239
- Franx, M., Illingworth, G.D., Kelson, D.D., Van Dokkum, P.G., Tran, K.-V., 1997 ApJL, 486, L75
- Hamana, T., Futamase, T., 1997, MNRAS 286, L7 (HF97)
- Hammer, F., 1991, ApJ 383, 66
- Hattori, M., Kenib, J.-P., Makino, N., 1999, Progress of Theoretical Physics, Supplement, 133, 1
- Hattori, M., Matuszawa, H., Morikawa, K., Kneib, J.-P., Yamashita, K., Watanabe, K., Böhringer, H., Tsuru, T.G., 1998, ApJ in press; astro-ph/9803092
- Hattori, M., Watanabe, K., Yamashita, K. 1997, A&A 319, 764 (Paper I)
- Henry, J.P., 1997, ApJ 489, L1
- Henry, J.P., Henriksen, H.J. 1986, ApJ 301, 689
- Kauffmann, G., 1997, in *Galaxy Interactions at Low and High Redshift*, IAU Symposium 186
- Kim, K.-T., Tribble, P.C., Kronberg, P.P., 1991, ApJ 379, 80
- King, I., 1962, ApJL 174, L123
- Kneib, J.-P., Ellis, R.S., Smail, I., Couch, W.J., Sharples, R.M., ApJ 471, 643
- Kneib, J.-P., Mellier, Y., Fort, B., Mathez, G., 1993, A&A 273, 367
- Kneib, J.-P., Mellier, Y., Pelló, R., Miralda-Escudé, J., Le Borgne, J.-F., Böhringer, H., Picat, J.-P., 1995 A&A 303, 27
- Le Fèvre, O., Hammer, F., Angonin, M.C., Gioia, I.M., Luppino, G.A., 1994, ApJL 422, L5 (LF94)
- Lilly, S.J., Tresse, L., Hammer, F., Crampton, D., Le Fèvre, O., 1995, ApJ 455, 108
- Lin, H., Kirshner, R.P., Shectman, S.A., Landy, S.D., Oemler, A., Tucker, D.L., Schechter, P.L., 1996, ApJ 464, 60
- Loeb, A., Mao, S., 1994, ApJL 435, L17
- Loveday, J., Peterson, B.A., Efstathiou, G., Maddox, S.J. 1992, ApJ 390, 338
- Lubin, L.M., Bahcall, N.A., 1993, ApJL 415, L17
- Luppino, G.A., Gioia, I.M., 1992, A&A 265, L9
- Lynds, R., Petrosian V. 1986, BAAS 18,1014
- Madau, P., Ferguson, H.C., Dickinson, M.E., Giavalisco, M., Steidel, C.C., Fruchter, A. 1996, MNRAS 283, 1388
- Makino, N., Sasaki, S., Suto Y., 1998, ApJ 497, 555
- Markevitch, M., 1998, ApJ submitted; astro-ph/9802059
- Miralda-Escudé, J., 1993a, ApJ 403, 497
- Miralda-Escudé, J., 1993b, ApJ 403, 509
- Miralda-Escudé, J., Babul, A., 1995, ApJ 449, 18
- Morris, S.L., Hutchings, J.B., Carlberg, R.G., Yee, H.K.C., Ellingson, E., Balogh, M.L., Abraham, R.G., Smecker-Hane T.A., 1998, ApJ in press;astro-ph/9805216
- Mushotzky, R.F., Scharf, C.A., 1997, ApJL 482, L13
- Narayan, R., Bartelmann, M., in *Formation of Structure in the Universe*, Proceedings of the 1995 Jerusalem Winter School, ed A. Dekel and J.P. Ostriker (Cambridge University Press)
- Navarro, J.F., Frenk, C.S., White, S.D.M., 1996, ApJ 462, 563 (NFW)
- Navarro, J.F., Frenk, C.S., White, S.D.M., 1997, ApJ 490, 493 (NFW)
- Neumann, D.M., Böhringer, H., 1997, MNRAS 289, 123 (NB97)
- Noguchi, M., 1997, in *Galaxy Interactions at Low and High Redshift*, IAU Symposium 186
- Pence, W., 1976, ApJ 203, 39
- Pierre, M., Le Borgne, J.F., Soucail, G., Kneib, J.-P., 1996, A&A 311, 413
- Roche, N., Ratnatunga, K., Griffiths, R.E., Im, M., Naim, A., 1998, MNRAS 293, 157
- Seitz, S., Saglia, R.P., Bender, R., Hopp, U., Belloni, P., Ziegler, B., 1997, MNRAS submitted; astro-ph/9706023
- Soucail, G., Fort, B., Mellier, Y., Picat, J.P., 1987, A&A 172, L14
- Soucail, G., Mellier, Y., Fort, B., Mathez, G., Cailloux, M., 1988, A&A 191, L19
- Totani, T., Yoshii, T., Sato, K. 1997, ApJ 483, L75
- Trümper, J., 1984, Physica Scripta 7, 209
- Umetsu, K., Tada, M., Futamase, T., 1999, Progress of Theoretical Physics, Supplement, 133
- Wu, X.-P., Hammer, F., 1993, MNRAS 262, 187
- Yoshii, Y., Takahara, F., 1988, ApJ 326, 1
- Yoshii, Y., Perterson B.A., 1991, ApJ 372, 8
- Zucca, E., Zamorani, G., Vettolani, G., Cappi, A., Merighi, R., Mignoli, M., Stirpe, G.M., MacGillivray, H. et al., 1997 A&A 326, 477